

See discussions, stats, and author profiles for this publication at: <https://www.researchgate.net/publication/23915580>

# Numerical Modeling of Thermofluid Transients During Chilledown of Cryogenic Transfer Lines

Article in SAE Technical Papers · February 2003

DOI: 10.4271/2003-01-2662 · Source: NTRS

---

CITATIONS

7

---

READS

320

2 authors, including:



[Alok Majumdar](#)

NASA

74 PUBLICATIONS 339 CITATIONS

SEE PROFILE

# Numerical Modeling of Thermofluid Transients During Chillover of Cryogenic Transfer Lines

**Alok Majumdar**

NASA Marshall Space Flight Center, MSFC, Alabama

**Todd Steadman**

Jacobs Sverdrup Technology, Inc., Huntsville, Alabama

Copyright © 2003 SAE International

## ABSTRACT

This paper describes the application of a finite volume procedure for a fluid network to predict thermofluid transients during chillover of cryogenic transfer lines. The conservation equations of mass, momentum, and energy and the equation of state for real fluids are solved in a fluid network consisting of nodes and branches. The numerical procedure is capable of modeling phase change and heat transfer between solid and fluid. This paper also presents the numerical solution of pressure surges during rapid valve opening without heat transfer. The numerical predictions of the chillover process have been compared with experimental data.

## INTRODUCTION

The chillover of fluid transfer lines is an important part of using cryogenic systems, such as those found in both ground- and space-based applications. The chillover process is a complex combination of both thermal and fluid transient phenomena. A cryogenic liquid flows through a transfer line that is initially at a much higher temperature than the cryogen. Transient heat transfer processes between the liquid and transfer line cause vaporization of the liquid, and this phase change can cause transient pressure and flow surges in the liquid. As the transfer line is cooled, these effects diminish until the liquid reaches a steady flow condition in the chilled transfer line. If these transient phenomena are not properly accounted for in the design process of a cryogenic system, it can lead to damage or failure of system components during operation. For such cases, analytical modeling is desirable for ensuring that a cryogenic system transfer line design is adequate for handling the effects of a chillover process. Since 1960, several analytical investigations to model chillover of cryogenic transfer lines were reported in literature. Burke et al. developed a single control volume model to predict

chillover time of a long stainless steel tube by flowing liquid nitrogen ( $LN_2$ ). [1] Chi developed an analytical model of the chillover under the assumptions of constant flow rate, constant heat transfer coefficient, and constant fluid properties. [2] Steward et al. modeled chillover numerically using a finite difference formulation of the one-dimensional, unsteady mass, momentum, and energy equation. [3] Heat transfer coefficients were determined using superposition of single-phase forced convection correlations and pool boiling correlations for both nucleate and film boiling. In recent years, a task has been undertaken at Marshall Space Flight Center to develop the Generalized Fluid System Simulation Program (GFSSP). GFSSP is a robust general fluid system analyzer, based on the finite volume method, with the capability to handle phase change, heat transfer, chemical reaction, rotational effects, and fluid transients in conjunction with subsystem flow models for pumps, valves, and various pipe fittings. [4] GFSSP has been extensively verified and validated by comparing its predictions with test data and other numerical methods for various applications, such as internal flow of turbo-pumps, [5] propellant tank pressurization, [6,7] and squeeze film damper rotordynamics. [8] GFSSP has also been used to predict the chillover of a cryogenic transfer line, based on transient heat transfer effects and neglecting fluid transient effects. [9] Recently, GFSSP's capability has been extended to include fluid transient effects. [10]

The purpose of this paper is to present the results of a numerical model developed using GFSSP's new fluid transient capability in combination with its previously developed thermal transient capability to predict pressure and flow surge in cryogenic transfer lines during a chillover process. An experiment performed by the National Bureau of Standards (NBS) in 1966 has been chosen as the baseline comparison case for this work. [11] NBS's experimental setup consisted of a 10.59-ft<sup>3</sup> (300-L) supply dewar, an inlet valve, and a 200-ft- (60.96-m-) long, 5/8-in- (1.59-cm-) inside

diameter (ID) vacuum jacketed copper transfer line that exhausted to atmosphere. Three different inlet valves, a 3/4-in (1.91-cm) port ball valve, a 1-in (2.54-cm) port globe valve, and a 1-in (2.54-cm) port gate valve, were used in NBS's experiments. Experiments were performed using both liquid hydrogen (LH<sub>2</sub>) and LN<sub>2</sub> as the fluids for several different conditions.

## MATHEMATICAL FORMULATION AND SOLUTION PROCEDURE

### FINITE VOLUME FORMULATION IN A FLUID NETWORK

Figure 1 shows a long pipeline connected to a tank with a valve placed at the beginning of the pipeline. Flow in a pipe may be considered as a series of discrete fluid nodes connected by branches. The numerical model consists of boundary nodes, internal nodes, and branches as shown in Figure 2. One boundary node represents the tank, and the other boundary node represents the ambient where the fluid is discharged. At the boundary nodes, pressure and temperature are specified. At the internal nodes, all scalar properties, such as pressure, temperature, density, compressibility factor, and viscosity, are computed. Mass flow rates are computed at the branches. Mass and energy conservation equations are solved at the internal nodes in conjunction with the thermodynamic equation of state while momentum conservation equations are solved at the branches.

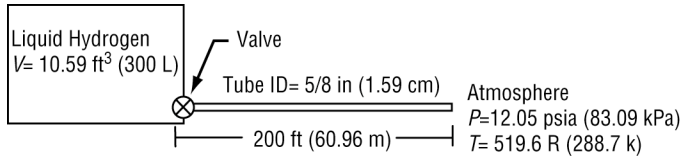


Figure 1. Hydrogen line chilldown experimental setup schematic.

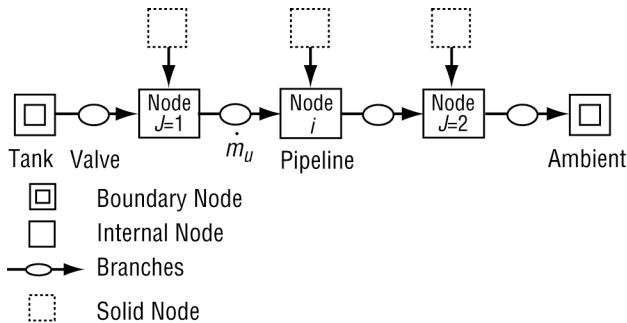


Figure 2. Network flow model of the fluid system consisting of tank, pipeline, and valve constructed with boundary nodes, internal nodes, solid nodes, and branches.

### Mass Conservation

The mass conservation equation at the  $i$ th node can be written as

$$\frac{m_{i+1} - m_i}{\Delta t} = \sum_{j=1}^n \dot{m}_{ij} \quad (1)$$

Equation (1) implies that the net mass flow from a given node must equate to rate of change of mass in the control volume. In the steady state formulation, the left side of the equation is zero. This implies that the total mass flow rate into a node is equal to the total mass flow rate out of the node.

### Momentum Conservation

The momentum conservation equation at the  $ij$  branch can be written as

$$\begin{aligned} & \frac{(mu)_{i+1} - (mu)_i}{g_c \Delta t} + \text{MAX}[\dot{m}_{ij}, 0] (u_{ij} - u_u) \\ & \quad \pm \text{MAX}[-\dot{m}_{ij}, 0] (u_{ij} - u_u) \\ & = (p_i - p_j) A_{ij} + \frac{\Delta g V \cos \theta}{g_c} \\ & \quad - K_f \dot{m}_{ij} |\dot{m}_{ij}| A_{ij} \end{aligned} \quad (2)$$

where the term  $\frac{(mu)_{i+1} - (mu)_i}{g_c \Delta t}$  represents Unsteady,  $\text{MAX}[\dot{m}_{ij}, 0] (u_{ij} - u_u) \pm \text{MAX}[-\dot{m}_{ij}, 0] (u_{ij} - u_u)$  represents Longitudinal Inertia,  $(p_i - p_j) A_{ij}$  represents Pressure,  $\frac{\Delta g V \cos \theta}{g_c}$  represents Gravity, and Friction is represented by  $K_f \dot{m}_{ij} |\dot{m}_{ij}| A_{ij}$ .

The left-hand side of the momentum equation represents the inertia of the fluid. The surface and body forces applied in the control volume are assembled in the right-hand side of the equation.

#### Unsteady

This term represents the rate of change of momentum with time. For steady state flow, the time step is set to an arbitrary large value and this term is reduced to zero.

#### Longitudinal Inertia

This term is important when there is a significant change in velocity in the longitudinal direction due to change in area and density. The MAX operator represents an upwind differencing scheme used to compute the velocity differential.

## Pressure

This term represents the pressure gradient in the branch. The pressures are located at the upstream and downstream face of a branch.

## Gravity

This term represents the effect of gravity. The gravity vector makes an angle ( $\theta$ ) with the assumed flow-direction vector. At  $\theta=180^\circ$ , fluid is flowing against gravity; at  $\theta=90^\circ$ , fluid is flowing horizontally, and gravity has no effect on the flow.

## Friction

This term represents the frictional effect. Friction was modeled as a product of  $K_f$  and the square of the flow rate and area.  $K_f$  is a function of the fluid density in the branch and the nature of the flow passage being modeled by the branch. For a pipe,  $K_f$  can be expressed as [4]

$$K_f = \frac{8fL}{\rho \theta^2 D^5 g_c} \quad (3)$$

For a valve,  $K_f$  can be expressed as [4,12]

$$K_f = \frac{\frac{K_1}{\text{Re}} + K \left( \frac{1}{D} + \frac{1}{D} \right)}{2g_c \rho A^2} \quad (4)$$

and for a generic resistance,  $K_f$  can be expressed as [4]

$$K_f = \frac{1}{2g_c \rho C_L^2 A^2} \quad (5)$$

## Energy Conservation

The energy conservation equation for node  $i$ , shown in Figure 2, can be expressed following the first law of thermodynamics and using enthalpy as the dependant variable. The energy conservation equation based on enthalpy can be written as

$$\begin{aligned} & \frac{m_i h_i - \frac{p_i}{\rho_i} \frac{dm_i}{dt} + \sum_{j=1}^n \left( m_{ij} h_{ij} - \frac{p_{ij}}{\rho_{ij}} \frac{dm_{ij}}{dt} \right)}{\rho_i} \\ &= \sum_{j=1}^n \left( \text{MAX}(\dot{m}_{ij}, 0) h_j - \text{MAX}(\dot{m}_{ij}, 0) h_i \right) + \dot{Q}_i \end{aligned} \quad (6)$$

where

$$\dot{Q}_i = h_c A (T_{\text{solid}} - T_{\text{fluid}}) \quad (6a)$$

The rate of increase of internal energy in the control volume is equal to the rate of energy transport into the control volume minus the rate of energy transport from the control volume. The MAX operator represents the upwind formulation.

## Equation of State

The resident mass in the  $i$ th control volume can be expressed from the equation of state for a real fluid as

$$m = \frac{pV}{RTz} \quad (7)$$

For a given pressure and enthalpy, the temperature and compressibility factor in Eq. (7) is determined from the thermodynamic property program developed by Hendricks et al. [13,14].

## Phase Change

Modeling phase change is fairly straightforward in the present formulation. Since a thermodynamic property program is integrated in the formulation, the vapor quality of a saturated liquid vapor mixture is calculated from

$$x = \frac{h - h_l}{h_v - h_l} \quad (8)$$

Assuming a homogeneous mixture of liquid and vapor, the density, specific heat, and viscosity are computed from the following relations:

$$\theta = (1-x)\theta_l + x\theta_v \quad (9)$$

where  $\theta$  represents specific volume, specific heat, or viscosity.

## Solid-to-Fluid Heat Transfer

Each internal fluid node is connected with a solid node as shown in Figure 2. The energy conservation equation for the solid node is solved in conjunction with all other conservation equations. The energy conservation equation for the solid can be expressed as

$$\begin{aligned} & \frac{(mC_p T_{\text{solid}})_{i+1} - (mC_p T_{\text{solid}})_i}{\rho_i} \\ &= h_c A (T_{\text{solid}} - T_{\text{fluid}}) \end{aligned} \quad (10)$$

The heat transfer coefficient of Eq. (10) is computed from the correlation given by Miropolskii: [15]

$$Nu = \frac{h_c D}{k_v} \quad (11)$$

where

$$Nu = 0.023 (Re_{mix})^{0.8} (Pr_V)^{0.4} (Y) , \quad (12)$$

$$Re_{mix} = (\rho u D / \mu_V) \left[ x + (\mu_V / \mu_I) (1 - x) \right] , \quad (13)$$

$$Pr_V = (C_p \mu_V / k_V) , \quad (14)$$

and

$$Y = 1 - 0.1 \frac{\mu_V}{\mu_I} \left( 1 - \frac{\mu_V}{\mu_I} \right)^{0.4} (1 - x)^{0.4} . \quad (15)$$

## SOLUTION PROCEDURE

The pressure, enthalpy, and resident mass in internal nodes and the flow rate in branches are calculated by solving Eqs. (1), (6), (7), and (2), respectively. A combination of the Newton-Raphson method and the successive substitution method has been used to solve the set of equations. The mass conservation (Eq. (1)), momentum conservation (Eq. (2)), and resident mass (Eq. (7)) equations are solved using the Newton-Raphson method. The energy (Eq. (6)) and specie (not discussed here) conservation equations are solved by the successive substitution method. The temperature, density, and viscosity are computed from pressure and enthalpy using a thermodynamic property program. [13,14] Figure 3 shows the simultaneous adjustment with successive substitution (SASS) scheme. The iterative cycle is terminated when the normalized maximum correction  $\Delta_{max}$  is less than the convergence criterion.  $\Delta_{max}$  is determined from

$$\Delta_{max} = \max \left| \frac{\sum_{i=1}^{N_E} \frac{\partial \Delta_i}{\partial \Delta_i}}{\Delta_i} \right| , \quad (16)$$

where  $\Delta$  is the dependent variable; e.g., pressure, flow rate, etc. The convergence criterion is set to 0.005 or less for the models presented in this paper. The details of the numerical procedure are described in Reference [4].

## RESULTS AND DISCUSSION

The development of the cryogenic transfer line chilldown model was performed in phases. The first phase involved constructing and utilizing the model to simulate the valve opening transient and cryogenic fluid filling the transfer line while neglecting heat transfer. The second phase involved including the effects of heat transfer in the model and comparing the model's predicted chilldown times with the experimental chilldown times reported by Brennan et al., [11] where chilldown time is defined as the time associated with the low-temperature

knee for a given transfer line wall temperature curve. Both phases of development have been completed, and their results are discussed below

The cryogenic transfer line model for the first phase is based on one of the experimental setups used by Brennan et al. [11] Figure 1 is a schematic of the experimental setup, which consists of a 200-ft- (60.96-m-) long, 5/8-in- (1.59-cm-) ID copper tube supplied by a 10.59-ft<sup>3</sup> (300-L) tank through a valve and exits to the atmosphere. The simulations for the first phase, discussed below, used LH<sub>2</sub>, supplied from the tank at 111.69 psia (770.07 kPa) and 35.43 R (19.7 K), as the cryogenic fluid. Figure 2 represents the numerical model that was created to simulate the LH<sub>2</sub> valve transient. The numerical model consists of 13 nodes (2 boundary nodes and 11 internal nodes) and 12 branches. The upstream boundary node represents the LH<sub>2</sub> tank while the downstream boundary node represents atmospheric conditions. The first branch represents the valve, the next 10 branches represent the transfer line, and the final branch provides an additional generic resistance that was needed to counter numerical problems that were encountered early in the modeling process.

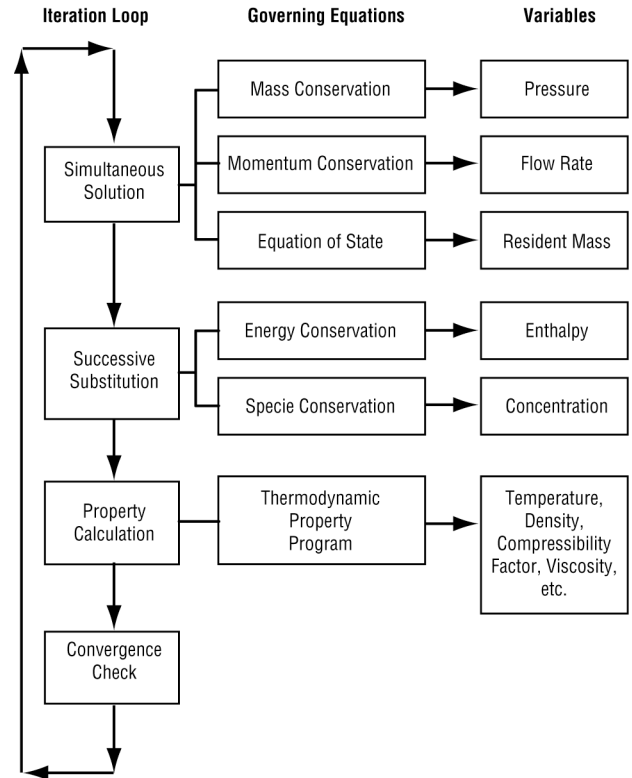


Figure 3. SASS scheme for solving governing equations.

Brennan et al. provide excellent detail with regard to their experimental setup in all regards except details concerning the different valves that were used. [11] They

provide neither the flow characteristics for the valve that they used, nor a history of the valve opening times that they simulated. In the absence of these data, assumptions were made concerning the flow characteristics of the valve based on the two-K method, [12] and two runs were performed with different valve opening times to gain a feel for the sensitivity of the model to opening time effects. The first run, designated a fast opening, involved an arbitrary 0.05-s transient. The second, or slow-opening run, used an arbitrary 0.5-s transient. Both transients were modeled assuming a linear change in flow area. Both models performed a 3-s simulation using a time step of 0.005 s. The model time step,  $\Delta t$ , was calculated using Eq. (17), such that the Courant number is greater than or equal to unity. For the case considered here,  $L_b=20$  ft (6.1 m) and  $a=3577$  ft/s (1090 m/s):

$$\text{Courant number} = \frac{L_b}{a \Delta t} \quad (17)$$

Figure 4 shows the pressure history for the fast-opening case. With no heat transfer effects, the model reaches a steady condition in <3 s. The maximum pressure transient for this case is 247 psia (1703 kPa) and is seen just downstream of the valve. Stations 1–4 are nodes whose locations approximately correspond to four instrument stations in the original experimental setup. [11] In the model, the stations are located at 20, 80, 140, and 200 ft (6.1, 24.38, 42.67, and 60.96 m), respectively, downstream of the tank. The propagation of the liquid front down the transfer line can be observed by examining the pressures at the four stations. The pressure increases as the liquid front approaches each station, forcing the hydrogen vapor initially in the transfer line toward the exit. When the liquid front reaches the station, a sharp pressure spike occurs, and a pressure wave propagates back toward the hydrogen tank, dampening out before it reaches the valve. The pressure spike is due to the complex interactions occurring at the liquid-vapor interface, including the resistance of the vapor to the liquid's momentum and condensation of some of the vapor in contact with the liquid. Some increased noise can be detected at each station prior to the initial pressure spike. This noise is thought to be a numerical artifact due to the complex interactions occurring at the node during that time.

Figure 5 shows the pressure history for the slow-opening case. A comparison of Figures 4 and 5 shows that the slower valve opening time affects the peak pressure by reducing its magnitude and shifting its location farther down the transfer line. In Figure 5, the peak pressure is  $\approx 193$  psia (1331 kPa) and occurs at Station 1. Naturally, the slower valve opening time slightly delays liquid propagation down the transfer line, but the character of the propagation is consistent in both cases.

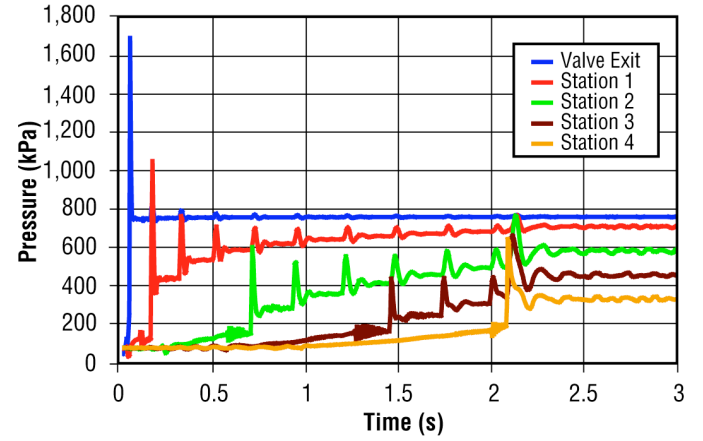


Figure 4. Transient pressure history for rapid valve opening.

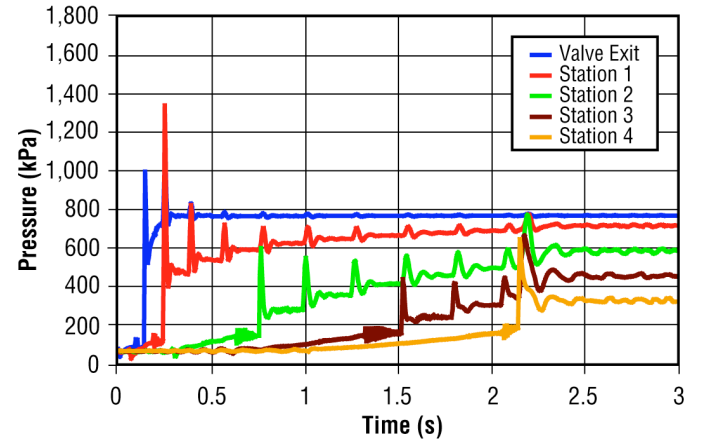


Figure 5. Valve transient pressure history for slow valve opening.

Figure 6 compares the wall temperatures of the 10- and 30-node transfer-line grid-resolution predictions of the numerical model and the experimental transfer-line wall temperatures published by Brennan et al. [11] over the course of a 90-s simulation. Each case is represented by a set of four curves corresponding to Stations 1–4 as discussed in the first-phase results above. It can be seen from Figure 6 that the time it takes for the liquid front to propagate to the exit significantly increases compared to the first-phase simulations. The decrease in inlet pressures between the first phase and second phase is a minor contributor to the slower liquid-propagation time, but the addition of heat transfer plays a much more significant role in slowing the propagation of the liquid front. This occurs because the transfer line is initially at a much higher temperature than the  $\text{LH}_2$ . As the valve opens, cold  $\text{LH}_2$  enters the transfer line and contacts the warm transfer-line wall. The  $\text{LH}_2$  not only experiences all of the complex interactions discussed above in the first-phase results, but also absorbs heat from the warm

transfer-line wall and vaporizes, which acts as a further impediment to the  $\text{LH}_2$  flow and causes the transfer line wall temperature to drop at Station 1. Stations 2–4 initially maintain a constant temperature, but as the transfer line wall cools at Station 1, more  $\text{LH}_2$ , mixed with cold gaseous hydrogen ( $\text{GH}_2$ ), is allowed to flow downstream, which causes the transfer-line wall temperatures to begin to drop at each successive station, as seen in Figure 6. This process occurs down the length of the transfer line until, eventually, the transfer-line wall has cooled to  $\text{LH}_2$  temperatures and the transfer line is completely filled with liquid.

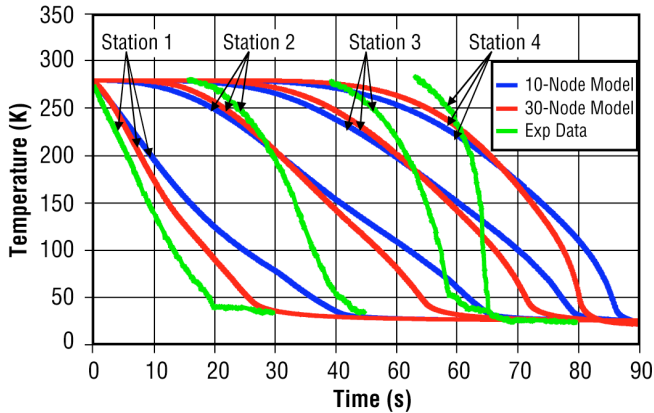


Figure 6. Tube wall-temperature history comparison with heat transfer effects.

It can be seen by comparing the three cases in Figure 6 that the model's predicted behavior agrees very well, qualitatively, with that observed by Brennan et al. in their experiments. [11] However, the initial second-phase simulations that were performed with a 10-node transfer-line grid resolution predict a chilldown time at Station 1 that is roughly 20 s slower than the experimental data, and a chilldown time at Station 4 that is roughly 23 s slower than that observed by the experiment. This discrepancy led to the decision to increase the transfer-line grid resolution from 10 to 30 nodes. The 30-node transfer-line grid-resolution model predicts a chilldown time at Station 1 that is roughly 8 s slower than the experimental data, and a chilldown time at Station 4 that is roughly 17 s slower than that observed by the experiment. While discrepancies still exist between the predicted and experimental chilldown times, the 30-node transfer-line grid-resolution results show a marked improvement in chilldown prediction time over the 10-node transfer-line grid-resolution model. One reason for the discrepancy in predicted chilldown time is that longitudinal conduction was not accounted for by this model, which can be seen in Figure 6 by noting that the discrepancy in predicted chilldown time increases at each successive station down the length of the transfer line.

Figures 7, 8 and 9 show the predicted pressure, vapor quality, and mass flow-rate histories for the 30-node model. Figure 7 shows that the pressure differential between the inlet and exit diminishes with time as vapor condenses in the transfer line. The jump in pressure near the exit, at 42 s, marks the onset of condensation near the transfer line inlet. The ramping down of all four pressure curves, at 80 s, is due to condensation throughout the transfer line. The condensation phenomenon is further evident in Figure 8, where the vapor quality at each station is plotted to show the progress of the liquid front down the transfer line. As the liquid front approaches each station, the vapor quality begins to drop. When the liquid front passes the station the quality reaches a zero or near-zero value. Figure 8 shows that by the end of the simulation, the transfer line is essentially completely filled with liquid. Figure 9 shows the predicted mass flow rates at the transfer line inlet, midpoint, and exit. As liquid enters the transfer line and propagates toward the exit, the mass flow rates increase, and after liquid has filled the entire transfer line, the mass flow rates converge on steady state values. Although the mass flow rate increases by a factor of 10 during the process, the spike seen in the exit mass flow rate, around 83 s, is believed to be numerical and not due to any physical process.

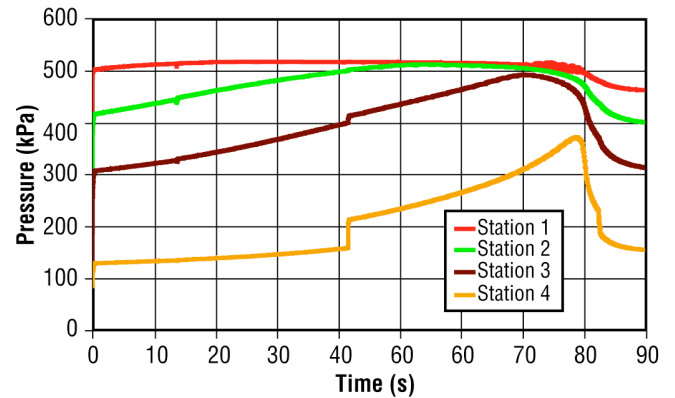


Figure 7. Fluid pressure history with heat transfer effects.

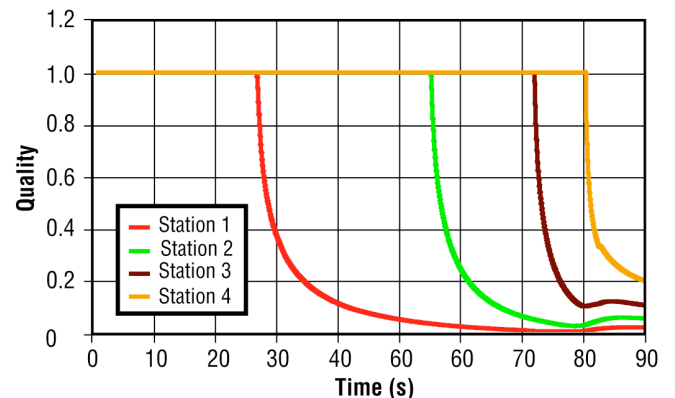


Figure 8. Fluid vapor-quality history with heat transfer effects.



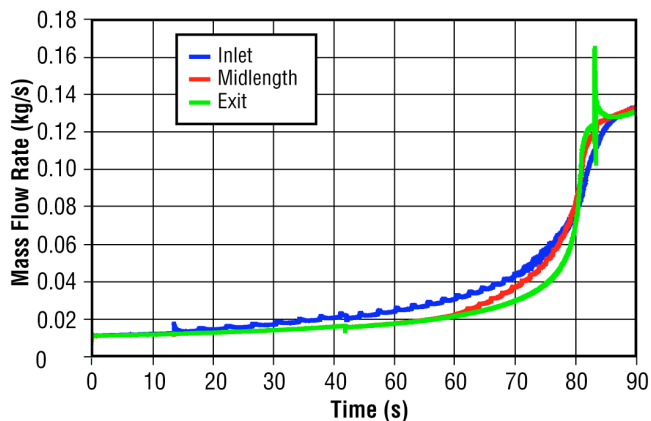


Figure 9. Fluid mass flow-rate history with heat transfer effects.

## CONCLUSIONS

In conclusion, a numerical model including both fluid transient and heat transfer effects has been developed to predict the chilldown of a long cryogenic transfer line. The developed numerical model was compared with experimental data, and it was found that increasing the grid resolution of the model was instrumental in improving the accuracy of the comparison. The numerical results also suggest that the chilldown of a long pipeline is a process where fluid flow and heat transfer are very strongly coupled. This is evident by observing that the mass flow rate increases by a factor of 10 during the chilldown process. A proper verification of a numerical model, as presented in this paper, will require more experimental data on transient-flow history. It is also felt that the inclusion of longitudinal conduction between solid nodes in the numerical model will further increase the accuracy of the model predictions.

## REFERENCES

- Burke, J.C.; Byrnes, W.R.; Post, A.H.; and Ruccia, F.E.: "Pressurized Cooldown of Cryogenic Transfer Lines," *Advances in Cryogenic Engineering*, Vol. 4, 1960, pp. 378–394.
- Chi, J.W.H.: "Cooldown Temperatures and Cooldown Time During Mist Flow," *Advances in Cryogenic Engineering*, Vol. 10, 1965, pp. 330–340.
- Steward, W.G.; Smith, R.V.; and Brennan, J.A.: "Cooldown Transients in Cryogenic Transfer Lines," *Advances in Cryogenic Engineering*, Vol. 15, 1970, pp. 354–363.
- Majumdar, A.K.: "A Second Law Based Unstructured Finite Volume Procedure for Generalized Flow Simulation," Paper No. AIAA 99-0934, 37th AIAA Aerospace Sciences Meeting Conference and Exhibit, January 11–14, 1999, Reno, NV.
- Van Hooser, K.; Bailey, J.W.; and Majumdar, A.K.: "Numerical Prediction of Transient Axial Thrust and Internal Flows in a Rocket Engine Turbopump," Paper No. 99-2189, 35th AIAA/ASME/SAE/ASEE Joint Propulsion Conference, June 20–24, 1999, Los Angeles, CA.
- Majumdar, A.K.; and Steadman, T.: "Numerical Modeling of Pressurization of a Propellant Tank," *J. of Propulsion and Power*, Vol. 17, No. 2, 2001, pp. 385–390.
- Steadman, T.; Majumdar, A.K.; and Holt K.: "Numerical Modeling of Helium Pressurization System of Propulsion Test Article (PTA)," 10th Thermal Fluid Analysis Workshop, September 13–17, 1999, Huntsville, AL.
- Schallhorn, P.A.; Elrod, D.A.; Goggin, D.G.; and Majumdar, A.K.: "Fluid Circuit Model for Long-Bearing Squeeze Film Damper Rotordynamics," *J. of Propulsion and Power*, Vol. 16, No. 5, 2000, pp. 777–780.
- Cross, M.F.; Majumdar, A.K.; Bennett Jr., J.C.; Malla, R.B.: "Modeling of Chill Down in Cryogenic Transfer Lines," *J. Spacecr. & Roc.*, Vol. 39, No. 2, 2002, pp. 284–289.
- Majumdar, A.K.; and Flachbart, R.H.: "Numerical Modeling of Fluid Transient by a Finite Volume Procedure for Rocket Propulsion Systems," Submitted for presentation at 2nd International Symposium on Water Hammer, 2003 ASME & JSME Joint Fluids Engineering Conference, July 6–10, Honolulu, Hawaii.
- Brennan, J.A.; Brentari, E.G.; Smith, R.V.; and Steward, W.G.: "Cooldown of Cryogenic Transfer Lines—An Experimental Report," National Bureau of Standards, November 1966.
- Hooper, W.B.: "The Two-K Method Predicts Head Losses in Pipe Fittings," *Chem. Engr.*, August 24, 1981, pp. 97–100.
- Hendricks, R.C.; Baron, A.K.; and Peller, I.C.: "GASP—A Computer Code for Calculating the Thermodynamic and Transport Properties for Ten Fluids: Parahydrogen, Helium, Neon, Methane, Nitrogen, Carbon Monoxide, Oxygen, Fluorine, Argon, and Carbon Dioxide," *NASA TN D-7808*, February, 1975.
- Hendricks, R.C.; Peller, I.C.; and Baron, A.K.: "WASP—A Flexible Fortran IV Computer Code for Calculating Water and Steam Properties," *NASA TN D-7391*, November 1973.
- Miropolskii, Z.L.: "Heat Transfer in Film Boiling of a Steam-Water Mixture in Steam Generating Tubes," *Teploenergetika*, Vol. 10, 1963, pp. 49–52; transl. AEC-tr-6252, 1964.

## NOMENCLATURE

**A** : Area (in<sup>2</sup>, m<sup>2</sup>)

**a** : Speed of sound (ft/s, m/s)

**C<sub>L</sub>** : Flow coefficient



**$C_p$** : Specific heat at constant pressure (Btu/lb-R, J/kg-K)

**$D$** : Diameter (in, cm)

**$f$** : Friction factor

**$g$** : Gravitational acceleration (=32.174 ft/s<sup>2</sup>, =9.81 m/s<sup>2</sup>)

**$g_c$** : Conversion constant (=32.174 lb-ft/lb<sub>f</sub>-s<sup>2</sup>)

**$h$** : Enthalpy (Btu/lb, J/kg)

**$h_c$** : Heat transfer coefficient (Btu/s-ft<sup>2</sup>-R, W/m<sup>2</sup>-R)

**$J$** : Mechanical equivalent of heat (= 778 ft-lb<sub>f</sub>/Btu)

**$K_f, K$** : Nondimensional head loss factor

**$K_f$** : Flow resistance coefficient (lb<sub>f</sub>-s<sup>2</sup>/(lb-ft)<sup>2</sup>, 1/kg-m)

**$k$** : Thermal conductivity (Btu/ft-s-R, W/m-K)

**$L$** : Length (in, m)

**$m$** : Resident mass (lb, kg)

**$\dot{m}$** : Mass flow rate (lb/s, kg/s)

**$N_E$** : Number of iterations

**$Nu$** : Nusselt number

**$Pr$** : Prandtl number

**$p$** : Pressure (lb<sub>f</sub>/in<sup>2</sup>, kPa)

**$\dot{Q}$** : Heat transfer rate (Btu/s, W)

**$R$** : Gas constant (lb<sub>f</sub>-ft/lb-R, N-m/kg-K)

**$Re$** : Reynolds number

**$T$** : Temperature (R, K)

**$u$** : Velocity (ft/s, m/s)

**$V$** : Volume (ft<sup>3</sup>, L)

**$x$** : Vapor quality

**$Y$** : Liquid-vapor mixture correlation factor

**$z$** : Compressibility factor

**$\Delta_{\max}$** : Normalized maximum correction

**$\Delta$** : Surface roughness of pipe (in, cm)

**$\Delta$** : Angle with gravity vector (deg)

**$\Delta$** : Viscosity (lb/ft-s, kg/m-s)

**$\Delta$** : Pi (=3.14159)

**$\Delta$** : Density (lb/ft<sup>3</sup>, kg/m<sup>3</sup>)

**$\Delta t$** : Time step (s)

**$t$** : Time (s)

**$\Delta$** : Dependant Variable (see Eqs. (9) and (16))

SUBSCRIPT

**$b$** : Branch

**$i$** :  $i$ th node

**$ij$** : Branch connecting  $i$ th &  $j$ th Nodes

**$j$** :  $j$ th node

**$l$** : Liquid

**$mix$** : Liquid-vapor mixture

**$u$** : Upstream

**$v$** : Vapor